Turbulent statistics and flow structures in spanwise-rotating turbulent plane Couette flows

Jie Gai
State Key Laboratory for Turbulence and Complex Systems, College of Engineering, Peking University, Beijing 100871, China

Zhenhua Xia*
Department of Engineering Mechanics, Zhejiang University, Hangzhou 310027, China and State Key Laboratory for Turbulence and Complex Systems, College of Engineering, Peking University, Beijing 100871, China

Qingdong Cai†
State Key Laboratory for Turbulence and Complex Systems, Center for Applied Physics and Technology, College of Engineering, Peking University, Beijing 100871, China

Shiyi Chen
Department of Mechanics and Aerospace Engineering, South University of Science and Technology of China, Shenzhen 518055, China and State Key Laboratory for Turbulence and Complex Systems, Center for Applied Physics and Technology, College of Engineering, Peking University, Beijing 100871, China

(Received 10 February 2016; published 2 September 2016)

A series of direct numerical simulations of spanwise-rotating turbulent plane Couette flows at a Reynolds number of 1300 with rotation numbers Ro between 0 and 0.9 is carried out to investigate the effects of anticyclonic rotation on turbulent statistics and flow structures. Several typical turbulent statistics are presented, including the mean shear rate at the centerline, the wall-friction Reynolds number, and volume-averaged kinetic energies with respect to the secondary flow field, turbulent field, and total fluctuation field. Our results show that the rotation changes these quantities in different manners. Volume-averaged balance equations for kinetic energy are analyzed and it turns out that the interaction term acts as a kinetic energy bridge that transfers energy from the secondary flow to the turbulent fluctuations. Several typical flow regimes are identified based on the correlation functions across the whole channel and flow visualizations. The two-dimensional roll cells are observed at weak rotation $\mathrm{Ro} = 0.01$, where alternant clustering of vortices appears. Three-dimensional roll cells emerge around $\mathrm{Ro} \approx 0.02$, where the clustering of vortices shows the meandering and bifurcating behavior. For moderate rotation $0.07 \lesssim \mathrm{Ro} \lesssim 0.36$, well-organized structures are observed, where the herringbonelike vortices are clustered between streaks from the top view of three-dimensional flow visualization and form annuluses. More importantly, the vortices are rather confined to one side of the walls when $\mathrm{Ro} \leqslant 0.02$ and are inclined from the bottom to upper walls when $\mathrm{Ro} \geqslant 0.07$.

DOI: 10.1103/PhysRevFluids.1.054401

I. INTRODUCTION

Owing to the presence of the Coriolis force, the shear flow may be either stabilizing or destabilizing in a rotating reference frame depending on the direction of rotation. If the system rotation has opposite

*xiazh1006@gmail.com
†caiqd@pku.edu.cn

sign to the mean flow vorticity, the flow becomes destabilized (anticyclonic rotation). In contrast, the flow is stabilized (cyclonic rotation) if they are of the same sign. In a spanwise-rotating plane Poiseuille flow, the Coriolis force acts in such a way that in part of the channel the flow becomes destabilized, whereas in the other part the flow stabilizes, since the mean vorticity changes its sign across the channel. However, in a spanwise-rotating plane Couette flow (RPCF) subject to a constant angular velocity Ω_z in the spanwise direction, the flow is either stabilizing or destabilizing across the whole channel. When the mean flow vorticity is antiparallel to the spanwise direction, a positive rotation number $\mathrm{Ro} = 2\Omega_z h/U_w > 0$ (U_w is half of the wall velocity difference and h is the half-channel height) means destabilizing rotation (anticyclonic rotation), while $\mathrm{Ro} < 0$ stands for stabilizing rotation (cyclonic rotation) [1,2].

In the past, great effort has been devoted to the study of the effect of system rotation on the flow behavior in RPCF, through both experiments and numerical simulations. Tillmark and Alfredsson [1] conducted experimental investigations on RPCF in both laminar and turbulent regimes and found that the stabilizing rotation ($\mathrm{Ro} < 0$) can relaminarize a turbulent flow. A linear relation between the transition Reynolds number $\mathrm{Re}_w = U_w h/\nu$ (ν is the kinematic viscosity) and rotation number Ro was obtained in the (Ro,Re_w) plane for stabilizing rotation and regularly spaced streamwise roll cells were observed in turbulence at $\mathrm{Re}_w \approx 700$ and $\mathrm{Ro} \approx 0.1$. Experimental observations of transitions and instabilities in RPCF have also been carried out by Alfredsson and Tillmark [2] and by Hiwatashi *et al.* [3]. Tsukahara *et al.* [4] extended previous experimental studies and reported systematic experimental investigations on RPCF. More than 400 observations, which were taken in the ranges of $0 < \mathrm{Re}_w < 1050$ and $-27 < \Omega < 30$ (here $\Omega = 2\Omega_z h^2/\nu = \mathrm{Re}_w \mathrm{Ro}$ is also a rotation number), were made to obtain a diagram that distinguishes various flow structures identified by the flow visualizations and 17 different flow regimes were identified, both laminar and turbulent with and without roll cells, as well as the transitional state where both laminar and turbulent regions can be observed at the same time. In particular, at turbulent state with higher Re_w, the flow structures related to roll cells undergo several different flow regimes as Ω increases, including a "featureless" regime at weak positive rotation or moderate negative rotation, where the flow lacks any apparent roll cells except vortical structures, a stable two-dimensional (2D) roll-cell regime, a spatial-temporal developing 3D roll-cell regime, and a stable 3D roll-cell regime. Furthermore, contained turbulence in the roll-cell regimes for both 3D roll cells and 2D meandering roll cells were observed in their experiments. However, all observations were based on 2D photographs and no flow structures were shown in real three dimensions. Also, the highest Reynolds number applied in the experiments of Tsukahara *et al.* [4] was limited to 1050.

Direct numerical simulation (DNS) is a popular approach to investigate the structures and statistics in RPCF. Bech and Andersson [5] performed DNS to investigate the turbulent RPCF at $\mathrm{Re}_w = 1300$ with the rotation numbers $\mathrm{Ro} = 0$, 0.01, 0.1, 0.2, and 0.5. They found that the roll-cell patterns at rotation numbers of 0.1 and 0.2 were far more regular and more energetic than those at a weak rotation rate $\mathrm{Ro} = 0.01$. At a higher rotation rate $\mathrm{Ro} = 0.5$, however, roll cells broke down and the turbulent field was enhanced. In another work Bech and Andersson [6] reported the DNS results of RPCF at weak rotation numbers $\mathrm{Ro} = \pm 0.01$ for $\mathrm{Re}_w = 1300$ and compared the results with the nonrotating case. They found that the destabilized flow was more energetic, but less three dimensional, than the nonrotating case, since the 2D roll cells extracted a comparable amount of kinetic energy from the mean flow. They also indicated that the turbulence anisotropy was unaffected by weak spanwise rotation and the secondary flow was highly anisotropic. Bech and Andersson [7] paid attention to the strong rotation $\mathrm{Ro} = 0.1$, 0.2, and 0.5 for $\mathrm{Re}_w = 1300$. Two flow regimes at strong rotation, that is, the regime of roll cells (or secondary streamwise vorticity), high wall shear stress, and low turbulence intensity and the regime of streamwise turbulent vortices from the anticyclonic wall layer, were identified. Furthermore, they reported that the maximum destabilization occurred at $\mathrm{Ro} \simeq 0.2$. At a sufficiently strong rotation number $\mathrm{Ro} = 0.7$ for $\mathrm{Re}_w = 1300$, Barri and Andersson [8] indicated that the roll-cell instability was completely suppressed, but the turbulence still persisted. Tsukahara [9] simulated RPCF at a Reynolds number of $\mathrm{Re}_w = 750$ to investigate the structures and turbulent statistics at different rotation numbers ($\mathrm{Ro} = 0$, ± 0.027, ± 0.04, and

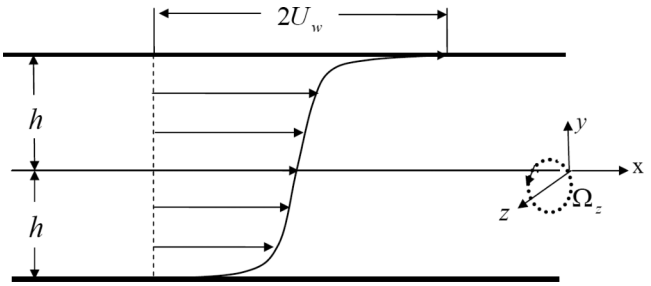

FIG. 1. Sketch of the flow geometry in RPCF.

± 0.06). The simulated flow structures were consistent with the former experimental observations by Tsukahara *et al.* [4], including the 3D roll-cell flow and contained turbulence in the roll-cell flow where small-scale eddies were concentrated inside the roll cells. Salewski and Eckhardt [10] used a set of progressively higher Reynolds numbers ($\mathrm{Re}_w = 650$, 1300, 2600, and 5200) to investigate the changes of momentum flux, measured by the wall shear stress, as a function of the rotation number in the range $-0.04 \leqslant \mathrm{Ro} \leqslant 0.6$. They found that the momentum flux for a given Re_w was a nonmonotonic function of rotation number. A single maximum was observed at low to moderate Reynolds numbers, while two maximums could be discerned at higher Reynolds numbers, at which the second stronger maximum emerged at smaller rotation number.

Despite of the numerous investigations of RPCF in the previous publications, the results were rather scattered and detailed work was rarely conducted to probe into a complete understanding of effect of Ro on both turbulent statistics and flow structures. Tsukahara *et al.* [4] depicted a rather complete phase diagram on flow structures based on 2D experimental photographs. However, no detailed flow statistics were reported therein. Bech and Andersson [5–7] and Barri and Andersson [8] reported flow statistics at no more than four sets of rotation numbers. However, the related flow structures were seldom discussed. In the present work, we carry out 20 DNSs of RPCF at $\mathrm{Re}_w = 1300$ with rotation numbers Ro between 0 and 0.9. We aim to explore a complete picture of the effects of the destabilizing rotation (anticyclonic rotation) on turbulent statistics and flow structures. The remainder of the paper is organized as follows. Details on numerical methods and validations are provided in Sec. II. The turbulent statistics and flow structures in RPCF will be presented and analyzed in Sec. III. A summary is given in Sec. IV.

II. NUMERICAL METHODS AND VALIDATIONS

Figure 1 shows a schematic plot of RPCF, where the top wall moves in the streamwise direction with a speed of $2U_w$ and the bottom wall is fixed. Two walls are separated by $2h$. The system is rotated about the z axis with a constant angular velocity Ω_z. Here u, v, and w (or u_1, u_2, and u_3) denote the instantaneous velocities in the streamwise (x), wall-normal (y), and spanwise (z) directions respectively. The momentum and continuity equations with constant fluid density ρ for this problem are

$$\frac{\partial u_i}{\partial t} + u_k \frac{\partial u_i}{\partial x_k} = -\frac{1}{\rho}\frac{\partial p}{\partial x_i} + \nu \frac{\partial^2 u_i}{\partial x_k^2} + 2\Omega_z \epsilon_{ik3} u_k, \tag{1}$$

$$\frac{\partial u_k}{\partial x_k} = 0, \tag{2}$$

where p is the effective pressure with the centrifugal effect absorbed. With reference velocity U_w and length scale h, the two characteristic parameters of this flow, i.e., Reynolds number Re_w and

TABLE I. Parameters of simulations at $\mathrm{Re}_w = 1300$: rotation number Ro, wall-friction Reynolds number Re_τ, wall-parallel spatial resolutions in viscous length scale Δx^+ and Δz^+, nondimensional time duration for statistics $U_w T/L_x$, nondimensional mean shear rate at the centerline $h\Psi/U_w$ and its standard deviation $h\sigma/U_w$, volume-averaged kinetic energy of total fluctuations $[k]_y$, kinetic energy with respect to secondary flow $[k^s]_y$, and kinetic energy of the turbulent field $[k'']_y$.

Case	Re_τ	Δx^+	Δz^+	$\frac{U_w T}{Lx}$	$\frac{h\Psi}{U_w}$	$\frac{h\sigma}{U_w} \times 10^2$	$\frac{[k]_y}{u_\tau^2\vert_{\mathrm{Ro}=0}}$	$\frac{[k^s]_y}{u_\tau^2\vert_{\mathrm{Ro}=0}}$	$\frac{[k'']_y}{u_\tau^2\vert_{\mathrm{Ro}=0}}$
Ro = 0	82.2	10.1	4.0	11.9	0.178	1.38	3.60	0.14	3.46
Ro = 0.005	83.5	10.2	4.1	6.37	0.075	1.56	4.13	1.20	2.92
Ro = 0.01	84.8	10.4	4.2	6.37	0.027	2.30	4.24	1.46	2.78
Ro = 0.02	87.7	10.8	4.3	6.37	−0.013	1.94	4.51	2.25	2.26
Ro = 0.04	98.1	12.0	4.8	6.37	0.027	0.90	6.09	4.59	1.50
Ro = 0.05	100.5	12.3	4.9	6.37	0.047	1.16	6.34	4.58	1.76
Ro = 0.07	103.7	12.7	5.1	6.37	0.077	0.91	6.85	5.48	1.36
Ro = 0.1	106.0	13.0	5.2	6.37	0.111	0.74	7.59	6.32	1.27
Ro = 0.15	107.7	13.2	5.3	6.37	0.155	0.65	8.72	7.32	1.39
Ro = 0.2	106.2	13.0	5.2	6.37	0.203	1.43	9.03	7.33	1.70
Ro = 0.25	104.4	12.8	5.1	6.37	0.253	1.59	9.51	7.54	1.97
Ro = 0.28	102.4	12.6	5.0	6.37	0.273	1.15	8.95	6.53	2.41
Ro = 0.32	99.6	12.2	4.9	15.9	0.295	1.19	8.05	5.20	2.85
Ro = 0.36	96.8	11.9	4.7	6.37	0.321	1.13	7.06	3.76	3.30
Ro = 0.4	94.2	11.6	4.6	6.37	0.353	1.23	6.32	2.36	3.95
Ro = 0.5	89.6	11.0	4.4	3.18	0.471	1.26	5.30	0.44	4.87
Ro = 0.6	83.1	10.2	4.1	6.37	0.576	1.05	4.68	0.08	4.60
Ro = 0.7	74.9	9.2	3.7	6.37	0.678	0.96	4.00	0.03	3.98
Ro = 0.8	64.1	7.9	3.1	6.37	0.782	0.92	2.99	0.03	2.96
Ro = 0.9	50.8	6.2	2.5	6.37	0.888	0.49	1.77	0.02	1.75

rotation number Ro, can be defined as

$$\mathrm{Re}_w = U_w h/\nu, \quad \mathrm{Ro} = 2\Omega_z h/U_w.$$

In the simulations, the incompressible Navier-Stokes equations (1) and (2) are solved by using the well-known algorithm proposed by Kim *et al.* [11], which is a pseudospectral method with Fourier and Chebyshev polynomial expansions in the wall-parallel directions (streamwise and spanwise directions) and wall-normal direction, respectively. It should be stated that our numerical methods are different from those used by Bech and Andersson [6,7] (ECCLES, a second-order-accurate finite-difference code [12]) and Barri and Andersson [8] (MGLET, a second-order finite-volume code [13]). The equations are integrated in time by using a semi-implicit scheme, that is, a second-order Adams-Bashforth scheme for the nonlinear term and a second-order Crank-Nicolson scheme for the linear term. The nonlinear term is dealiased by using a 3/2-truncation rule. A no-slip condition is imposed at the walls and periodic boundary conditions are employed in the horizontal directions. In order to save computational time, the simulation for a particular Ro was initialized with a velocity field from the preceding simulation of lower rotation number, while the first nonrotating simulation was started from a laminar field imposed with divergence-free perturbations.

All present DNSs (see Table I) are run at a Reynolds number of $\mathrm{Re}_w = 1300$. The computational domain is chosen as $10\pi h \times 2h \times 4\pi h$ in the x, y, and z directions respectively, and the number of grid points is $256 \times 70 \times 256$. The computational domain and the number of grid points are the same as those used by Bech and Andersson [5–7,14]. However, the sampling time durations T in all of the present cases are longer than those used by Bech and Andersson [6,7]. In present work the sampling time interval ΔT is $0.125h/U_w \approx 0.004L_x/U_w$ and the time step dt is $0.0025h/U_w$. The wall-friction Reynolds number is $\mathrm{Re}_\tau = u_\tau h/\nu$, where the friction velocity u_τ is calculated

by $u_\tau = \sqrt{\tau_w/\rho}$, with ρ and τ_w being the density of the fluid and the magnitude of the wall shear stress, respectively. The spatial resolutions Δx^+ and Δz^+ are scaled with the viscous length scale $l_\nu = \nu/u_\tau$. The details regarding computational conditions are listed in Table I.

In the present study the following notation will be employed for the averaging and decomposition of the flow field. The average of an instantaneous flow variable $f(x,y,z,t)$ with respect to x, z, and time t is denoted by $\langle f\rangle(y)$ and $\overline{f}(y,z)$ denotes the average of $f(x,y,z,t)$ with respect to x and t. The fluctuations corresponding to $\langle f\rangle(y)$ and $\overline{f}(y,z)$ are f' and f'', respectively. Thus, the instantaneous velocity field u_i can be decomposed into three parts by using a triple-decomposition approach [6,15,16],

$$u_i(x,y,z,t) = \langle u_i\rangle(y) + u_i'(x,y,z,t) = \overline{u_i}(y,z) + u_i''(x,y,z,t) = \langle u_i\rangle(y) + u_i^s(y,z) + u_i''(x,y,z,t). \tag{3}$$

In unidirectional flow, the mean or background flow is $\langle u_i\rangle(y) = [\langle u\rangle(y),0,0]$. Here u_i^s is the velocity field corresponding to the secondary flow, usually occurring as roll cells, which is defined as

$$u_i^s(y,z) = \overline{u_i}(y,z) - \langle u_i\rangle(y). \tag{4}$$

For clarity, we call u_i' total fluctuations and u_i'' turbulent fluctuations [6]. According to the above definitions, u_i, u_i^s, and u_i'' satisfy the following properties:

$$\langle u_i\rangle = \langle\overline{u_i}\rangle; \quad \langle u_i^s\rangle = 0, \quad \overline{u_i^s} = u_i^s; \quad \langle u_i''\rangle = 0, \quad \overline{u_i''} = 0. \tag{5}$$

It should be commented that the triple decomposition might not be a proper decomposition method in a simulation where the positions of the streamwise vortices vary with time. However, if the periodic boundary conditions were applied on a finite computational box, as done in the present work, the positions of these vortices would probably be fixed, and this is true for most of the cases studied. Therefore, the triple decomposition can still serve as an analysis tool, especially when we focus on the effects on the rotation rates.

Following the same decomposition, the total kinetic energy $K \equiv \langle u_i u_i\rangle/2$ (the Einstein summation convention is used) can also be decomposed into three parts, i.e.,

$$K = \tfrac{1}{2}\langle u_i\rangle\langle u_i\rangle + \tfrac{1}{2}\langle u_i' u_i'\rangle \tag{6}$$

$$= \tfrac{1}{2}\langle u_i\rangle\langle u_i\rangle + \tfrac{1}{2}\langle u_i^s u_i^s\rangle + \tfrac{1}{2}\langle u_i'' u_i''\rangle. \tag{7}$$

Note that u_i^s and u_i'' are uncorrelated ($\langle u_i^s u_i''\rangle = \langle\overline{u_i^s u_i''}\rangle = \langle u_i^s\overline{u_i''}\rangle = 0$). Here $k'' \equiv \frac{1}{2}\langle u_i'' u_i''\rangle$, $k^s \equiv \frac{1}{2}\langle u_i^s u_i^s\rangle$, and $k \equiv \frac{1}{2}\langle u_i' u_i'\rangle = k'' + k^s$ are the turbulent kinetic energy, the kinetic energy of the secondary flow, and the kinetic energy of the total fluctuations, respectively. The corresponding volume-averaged quantities are denoted by $[k'']_y$, $[k^s]_y$, and $[k]_y$. Here $[\phi]_y$ is defined as

$$[\phi]_y = \frac{1}{2h}\int_{-h}^{h}\phi(y)dy.$$

In Fig. 2(a) we show the mean velocity profiles (scaled with the wall velocity difference $2U_w$) at Ro = 0.01, 0.2, and 0.7 from our present simulations. The previously published results from Bech and Andersson [6,7] at Ro = 0.01 and 0.2 and Barri and Andersson [8] at Ro = 0.7 are plotted for comparison. It can be observed that the first-order statistics, i.e., the mean velocity profiles, from our present simulations match very well with those from the preciously reported results, even though Barri and Andersson [8] used a larger computational box size in the streamwise direction and finer grid resolutions in the streamwise and wall-normal directions. The profiles of kinetic energy with respect to total fluctuations at Ro = 0.01 and 0.2 from the present simulations and from Bech and Andersson [6,7] are shown in Fig. 2(b); no obvious discrepancy can be detected. These two comparisons confirm the correctness and accuracy of the present simulations.

In order to further study the effects of computational box size in the streamwise direction and the grid resolution in the wall-normal direction, three additional DNSs have been performed, including

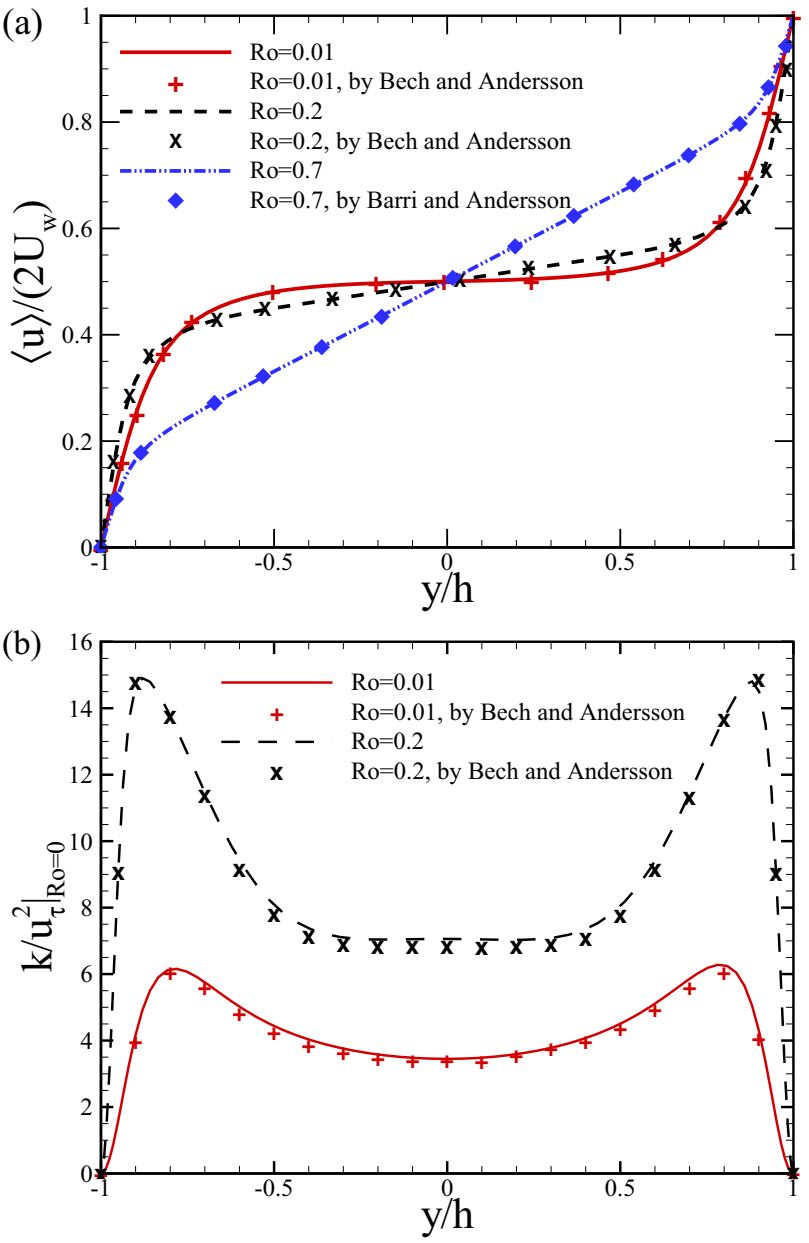

FIG. 2. (a) Mean velocity profiles $\langle u \rangle / 2U_w$ at Ro = 0.01, 0.2, and 0.7 and (b) kinetic energy of total fluctuations at Ro = 0.01 and 0.2 (scaled with u_τ^2 at Ro = 0). The previously published results from Bech and Andersson [6,7] for Ro = 0.01 and 0.2 and Barri and Andersson [8] for Ro = 0.7 are plotted for comparison.

the simulations at Ro = 0.01 (denoted by Ro = 0.01a) and 0.2 (denoted by Ro = 0.2a) with a much larger box $20\pi h \times 2h \times 4\pi h$ and the simulation at Ro = 0.2 (denoted by Ro = 0.2b) with a finer grid resolution in the wall-normal direction. The detailed parameters are listed in Table II. The mean velocity profiles from these three additional cases as well as the standard ones at Ro = 0.01 and 0.2 are shown in Fig. 3(a) and it is apparent that they match with the corresponding data very well. This illuminates that the computational box size in the streamwise direction and the grid resolution in

TABLE II. Parameters of the three additional DNSs at $\mathrm{Re}_w = 1300$. Here L_x, L_y and L_z are the streamwise, wall-normal, and spanwise lengths of the computational domain, respectively, and N_x, N_y, and N_z are the number of collocation points in the corresponding directions.

Case	Ro	Re_τ	Δx^+	Δz^+	$\frac{U_w T}{Lx}$	$\frac{U_w \Delta T}{Lx}$	$L_x \times L_y \times L_z$	$N_x \times N_y \times N_z$
$\mathrm{Ro} = 0.01a$	0.01	84.7	10.3	4.2	4.78	0.008	$20\pi h \times 2h \times 4\pi h$	$512 \times 70 \times 256$
$\mathrm{Ro} = 0.2a$	0.2	105.9	12.9	5.2	4.78	0.008	$20\pi h \times 2h \times 4\pi h$	$512 \times 70 \times 256$
$\mathrm{Ro} = 0.2b$	0.2	106.2	13.0	5.2	6.37	0.004	$10\pi h \times 2h \times 4\pi h$	$256 \times 128 \times 256$

the wall-normal direction will not cause any distinct differences in the mean velocity statistics. In Fig. 3(b) we show the profiles of k^s and k'' at $\mathrm{Ro} = 0.01$ and $\mathrm{Ro} = 0.2$ from different computational box sizes and grid resolutions. It is evident from the figure that the larger computational box size will result in a slight drop of k^s, while it will increase k'' slightly. The overall effect results in a little reduction in k ($k = k^s + k''$, not shown) and this reduction is more obvious for higher Ro, where the roll cells are more energetic. This is consistent with the common intuition that a larger streamwise length of the box will reduce the effect of the periodic boundary condition. On the other hand, an increase of grid points in the wall-normal direction will hardly induce any obvious changes in k^s, k'', and k. The slight or inconspicuous changes by using a larger computational box or finer wall-normal grid resolution further support the choice of the present resolution in the main study, as listed in Table I.

III. TURBULENT STATISTICS AND FLOW STRUCTURES

A. Turbulent statistics

Due to the system rotation, turbulent characteristics will change with Ro. Bech and Andersson [7] reported a number of profiles at $\mathrm{Ro} = 0$, 0.01, 0.1, 0.2, and 0.5, including the mean velocity, the vorticity ratio $S = 2\Omega_z/(-d\langle u\rangle/dy)$, and the anisotropy parameter $a = \langle v'v'\rangle/\langle u'u'\rangle - 1, k'', k^s$, and discussed the primary effects of system rotation. In this subsection we will not focus on these profiles, but report the changes of several characteristic statistics of the turbulence as a function of Ro.

The first statistic is the mean shear rate at the centerline $\Psi = d\langle u\rangle/dy|_{y=0}$ and its standard deviation σ, which is defined as

$$\sigma = \sqrt{\frac{1}{N_t}\sum_{i=1}^{N_t}\left(\frac{d[u(x,0,z,t_i)]_{x,z}}{dy} - \left.\frac{d\langle u\rangle}{dy}\right|_{y=0}\right)^2}. \tag{8}$$

Here $[\cdot]_{x,z}$ denotes quantities that are averaged in the x and z directions and $N_t = 1600$ at all rotation numbers. Nondimensional values of Ψ and σ are listed in Table I. Figure 4(a) shows the change of Ψ (scaled by U_w/h) as a function of Ro with σ (scaled by U_w/h) being the vertical error bars. Bech and Andersson [7] pointed out that Ψ decreased with Ro for $0 \leqslant \mathrm{Ro} \leqslant 0.01$ and increased with Ro when $0.1 < \mathrm{Ro} \leqslant 0.5$. This trend is consistent with our results. However, some information was missed in their work due to the limitation of rotation numbers studied. As can be seen from Fig. 4(a), Ψ decreases with Ro for $0 \leqslant \mathrm{Ro} \lesssim 0.02$ and increases with it when $\mathrm{Ro} > 0.02$. A minimum value is found at a rotation number around 0.02 and its value is slightly negative. The negative velocity gradient in the center of the channel was also reported in the recent experimental measurements conducted by Kawata and Alfredsson [17]. The vorticity ratio $S = 2\Omega_z/(-d\langle u\rangle/dy) = -\mathrm{Ro}/(hd\langle u\rangle/dy/U_w)$ is an important parameter to determine the stability behavior of the rotating shear flow based on the sign of the Bradshaw-Richardson number $B = S(S+1)$ [18]. According to the criterion, the case $S = -1$ should be neutrally stable (i.e., $B = 0$) just like the nonrotating case $S = 0$. In this case, the absolute vorticity $2\Omega_z - d\langle u\rangle/dy = 0$ and it is usually referred to as the zero-absolute-vorticity state [19,20]. Furthermore, the flow is destabilizing when $-1 < S < 0$ (or $B < 0$) and stabilizing otherwise. In Fig. 4(a) a dashed line with $h\Psi/U_w = \mathrm{Ro}$ [$S|_{y=0} = -\mathrm{Ro}/(h\Psi/U_w) = -1$] is also plotted for reference. Compared with

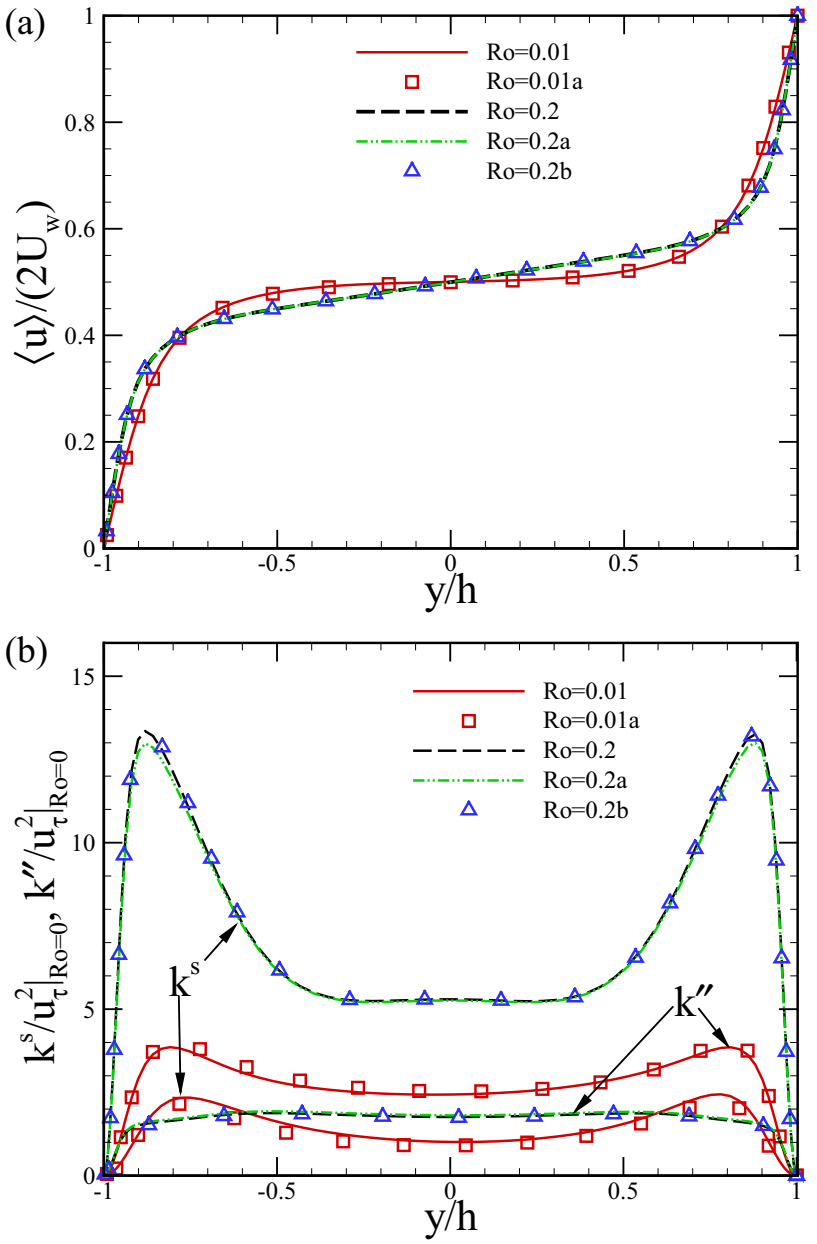

FIG. 3. Profiles of (a) $\langle u \rangle / 2U_w$ and (b) k^s and k'' (scaled with u_τ^2 at Ro $= 0$) at Ro $= 0.01$ and 0.2 with different computational box sizes and grid resolutions, including primary simulations Ro $= 0.01$ and 0.2 and three extra simulations Ro $= 0.01a$, $0.2a$, and $0.2b$, as listed in Tables I and II.

the line $h\Psi/U_w = \text{Ro}$ ($S|_{y=0} = -1$), it is found that the flow is destabilizing at the center line (i.e., $S|_{y=0} > -1$) for $0 \leqslant \text{Ro} \lesssim 0.01$ and $0.07 \leqslant \text{Ro} \lesssim 0.15$ and it is stabilizing at the centerline (i.e., $S|_{y=0} < -1$) for $0.02 \leqslant \text{Ro} \lesssim 0.05$ and $\text{Ro} \geqslant 0.32$. For $0.2 \leqslant \text{Ro} \leqslant 0.25$, the dimensionless mean shear rate at the centerline is almost equal to Ro (i.e., $S|_{y=0} = -1$), where the shear flow at the center plane is neutrally stable. This is consistent with the recent experimental finding that zero absolute vorticity can be established in the central parts of the channel in turbulent RPCF for high enough

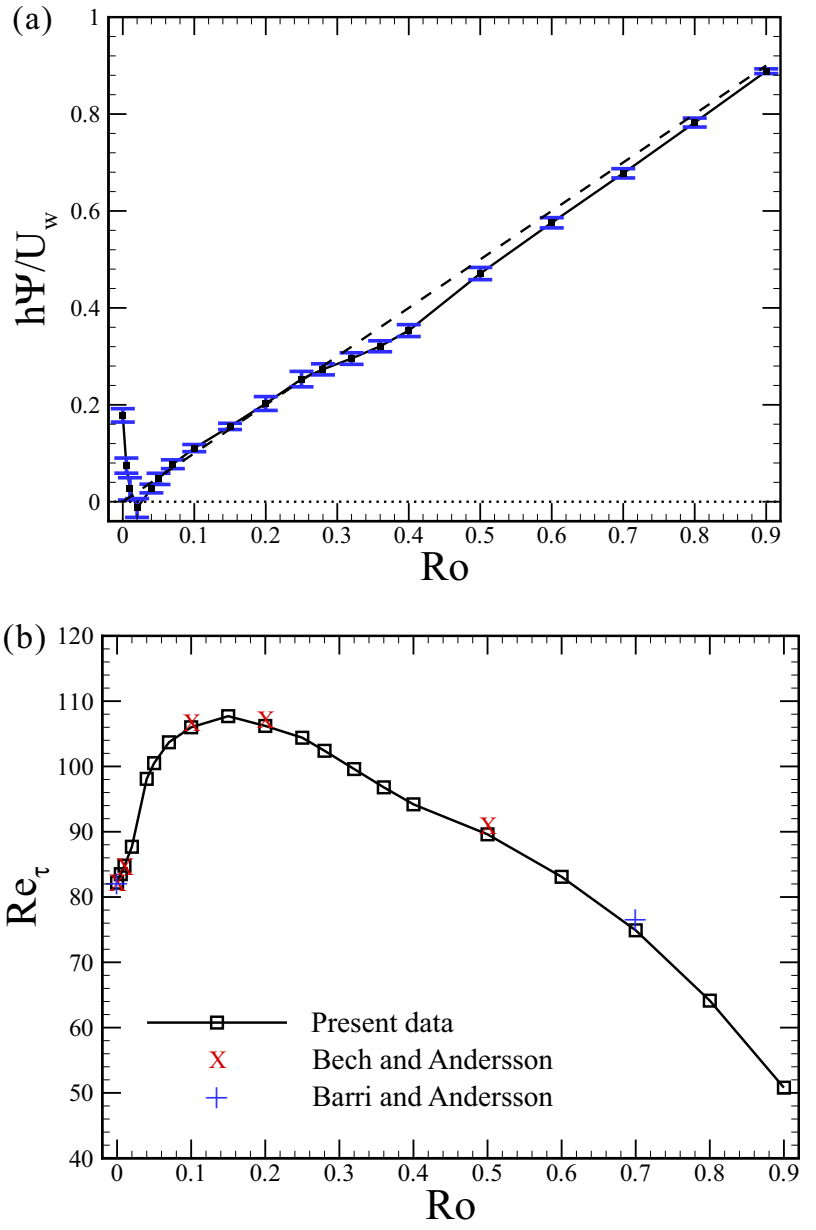

FIG. 4. (a) Change of $h\Psi/U_w$ as a function of Ro. The standard deviation σ defined by Eq. (8) is given as the vertical error bars (scaled by U_w/h). The dashed line denotes $h\Psi/U_w = \mathrm{Ro}$. (b) Wall-friction Reynolds number Re_τ as a function of Ro. The previously published results from Bech and Andersson [5] for Ro = 0, 0.01, 0.1, 0.2, and 0.5 and Barri and Andersson [8] for Ro = 0 and 0.7 are shown.

rotation rates [17]. In fact, Suryadi *et al.* [19] reported a similar figure of $h\Psi/U_w$ and Ro based on experimental measurements of spanwise-rotating laminar plane Couette flow at $\mathrm{Re}_w = 100$. They found that Ψ increases with Ro when $0.1 \lesssim \mathrm{Ro} \leqslant 0.9$ and it is slightly below the neutrally stable line, which corresponds to the zero absolute vorticity.

In Fig. 4(b) we show the wall-friction Reynolds number Re_τ as a function of Ro. The previously published results from Bech and Andersson [5] for Ro = 0, 0.01, 0.1, 0.2, and 0.5 and Barri and

Andersson [8] for Ro = 0 and 0.7 are also shown for reference. The results show that our data are in good agreement with those previously reported, which further confirms the accuracy of the present simulations. Since Re_w is fixed in the present study and $d(\langle u\rangle/U_w)/d(y/h)|_{y/h=-1} = \mathrm{Re}_\tau^2/\mathrm{Re}_w$, Re_τ can be used to indicate the mean shear rate at the wall or the wall friction. It is apparent that the mean shear rate at the wall shows an opposite trend to that at the centerline. That is, it first increases with Ro and then decreases with Ro. The maximum of Re_τ occurs at Ro ≈ 0.15, where its value is 31% larger than that of the nonrotating case and approximately 3 times that at the fully laminarized state at Ro = 1.0 [2,7] ($\mathrm{Re}_\tau = \sqrt{\mathrm{Re}_w}$ at Ro = 1.0). This corresponds to a 71.7% increase in wall friction as compared to the nonrotating case. At Ro ≈ 0.611 (a linear interpolation approximation), Re_τ returns to the value of the nonrotating case. After that, the rotation will reduce the wall friction. The change of Re_τ with Ro is similar to the result presented in Ref. [10], where only one single maximum was discerned. However, the peak in our work is located around Ro = 0.15 rather than the reported Ro = 0.2 by Salewski and Eckhardt [10]. This discrepancy can be attributed to the smaller computational box size and the very sparse rotation numbers at Ro $\geqslant 0.1$ in their study.

The second characteristic quantity is the volume-averaged kinetic energy. In Fig. 5(a) we display the volume-averaged kinetic energies $[k]_y$, $[k^s]_y$, and $[k'']_y$ as functions of Ro. The detailed values are listed in Table I. For $[k]_y$, it can be clearly seen that it first increases with Ro and then decreases with Ro. The turning point occurs around Ro = 0.25, which is close to the value Ro = 0.2 reported by Bech and Andersson [7]. Thus, the rotation first enhances the total fluctuations when Ro $\leqslant 0.25$ and then suppresses them when Ro > 0.25. A similar trend is also found in spanwise-rotating turbulent channel flow [21]. Here $[k^s]_y$ follows the same trend as $[k]_y$, while $[k'']_y$ shows the opposite trend for $0 \leqslant \mathrm{Ro} \leqslant 0.5$. The minimal $[k'']_y$ occurs around Ro = 0.1. Two intersections of $[k^s]_y$ and $[k'']_y$ exist in the rotation number range studied, illustrating that the secondary flows contribute half of the kinetic energy of the total fluctuations. One is around Ro = 0.02 and the other is within the range of $0.36 < \mathrm{Ro} < 0.4$. The kinetic energy of the secondary flow $[k^s]_y$ plays a dominant role in the range between two intersections. The ratios $[k^s]_y/[k]_y$ and $[k'']_y/[k]_y$ are shown in Fig. 5(b). It is interesting to notice that the contribution of the secondary flow to the kinetic energy of total fluctuations reaches a "saturation" level when $0.07 \lesssim \mathrm{Ro} \lesssim 0.25$, where the variations of $[k^s]_y/[k]_y$ are smaller than 5%. As the rotation increases, the secondary flow is fully suppressed by the strong system rotation when Ro $\gtrsim 0.7$, where $[k'']_y/[k]_y$ is very close to 1.0.

In order to gain more insight into the behavior of the kinetic energy with respect to the total fluctuations k, we study the changes of profiles about k with rotation numbers. The profiles of k at several rotation numbers are displayed in Fig. 6. We observe that when $0 \lesssim \mathrm{Ro} \lesssim 0.32$ the peaks of k are located near the wall, but when Ro $\gtrsim 0.4$ the peaks of k are located at the center plane. The distributions of k become convex functions when Ro $\gtrsim 0.4$ and it is caused by the dominant role of $\langle v'v'\rangle/2$ in the core region. Furthermore, the peak of k in the near wall region increases with Ro when $0 \lesssim \mathrm{Ro} \lesssim 0.15$ and decreases with Ro when Ro $\gtrsim 0.2$. When Ro $\gtrsim 0.25$, the values of k across the whole channel decrease gradually with Ro. It should be mentioned that the changes of profiles about k^s (not shown here) are very similar to those of k for $0 < \mathrm{Ro} < 0.6$ and this is consistent with the similar trends between $[k]_y$ and $[k^s]_y$.

The transport equations for k, k^s, and k'' are as follows:

$$\frac{Dk}{Dt} = \underbrace{-\langle u'v'\rangle\frac{d\langle u\rangle}{dy}}_{P}\underbrace{-\nu\left\langle\frac{\partial u_i'}{\partial x_j}\frac{\partial u_i'}{\partial x_j}\right\rangle}_{-\varepsilon} + \frac{d}{dy}\left[\nu\frac{dk}{dy} - \frac{1}{2}\langle u_i'u_i'v'\rangle - \frac{1}{\rho}\langle p'v'\rangle\right], \tag{9}$$

$$\frac{Dk^s}{Dt} = \underbrace{-\langle u^s v^s\rangle\frac{d\langle u\rangle}{dy}}_{P^s}\underbrace{-\nu\left\langle\frac{\partial u_i^s}{\partial x_k}\frac{\partial u_i^s}{\partial x_k}\right\rangle}_{-\varepsilon^s} + \underbrace{\left\langle\overline{u_i''u_k''}\frac{\partial u_i^s}{\partial x_k}\right\rangle}_{-Tr} + \frac{d}{dy}\left[\nu\frac{dk^s}{dy} - \frac{1}{2}\left\langle u_i^s u_i^s v^s\right\rangle - \frac{1}{\rho}\langle p^s v^s\rangle - \left\langle\overline{u_i''v''}u_i^s\right\rangle\right], \tag{10}$$

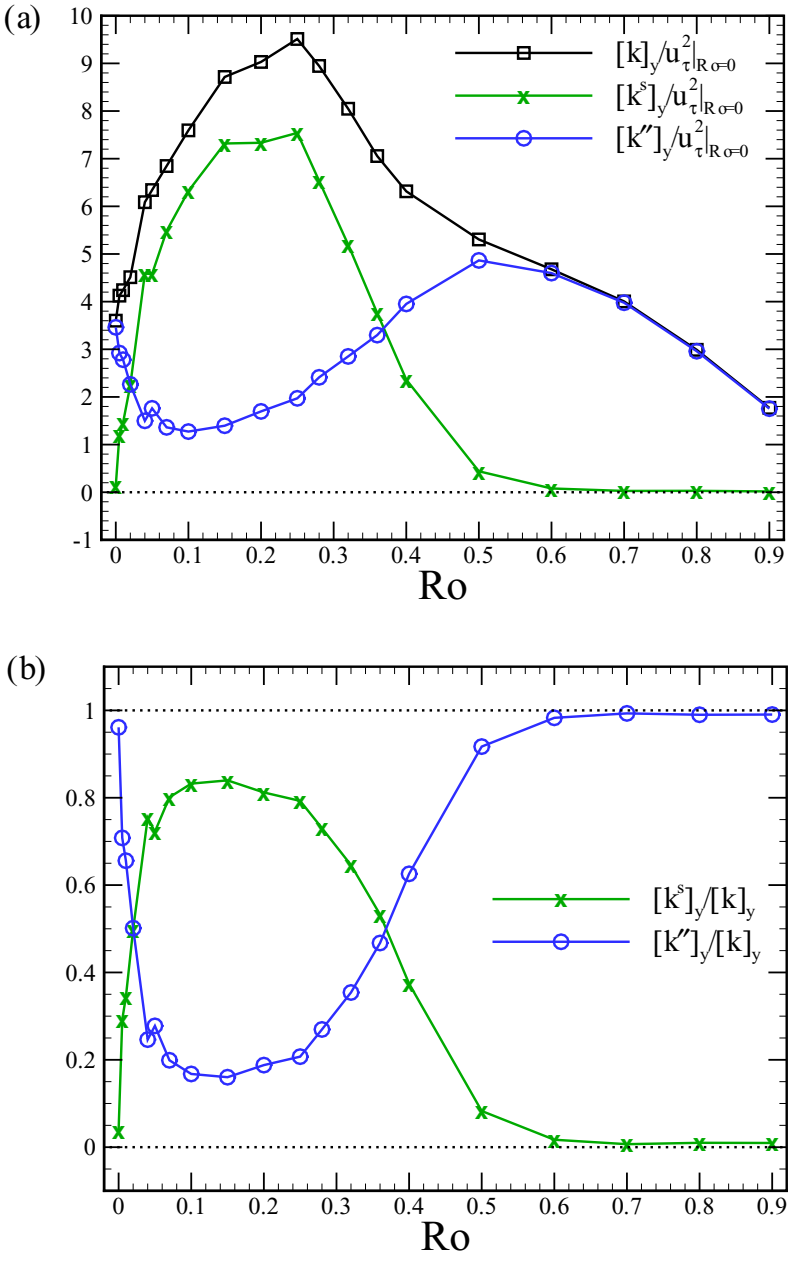

FIG. 5. (a) Volume-averaged kinetic energies $[k]_y$, $[k^s]_y$, and $[k'']_y$ as functions of Ro. All quantities are scaled with u_τ^2 at Ro = 0. (b) Ratios $[k^s]_y/[k]_y$ and $[k'']_y/[k]_y$ as functions of Ro.

$$\frac{Dk''}{Dt} = \underbrace{-\langle u''v''\rangle\frac{d\langle u\rangle}{dy}}_{P''}\underbrace{-\nu\left\langle\frac{\partial u_i''}{\partial x_k}\frac{\partial u_i''}{\partial x_k}\right\rangle}_{-\varepsilon''}\underbrace{-\left\langle\overline{u_i''u_k''}\frac{\partial u_i^s}{\partial x_k}\right\rangle}_{Tr}$$
$$+\frac{d}{dy}\left[\nu\frac{dk''}{dy}-\frac{1}{2}\langle u_i''u_i''v''\rangle-\frac{1}{\rho}\langle p''v''\rangle-\frac{1}{2}\langle\overline{u_i''u_i''}v^s\rangle\right]. \quad (11)$$

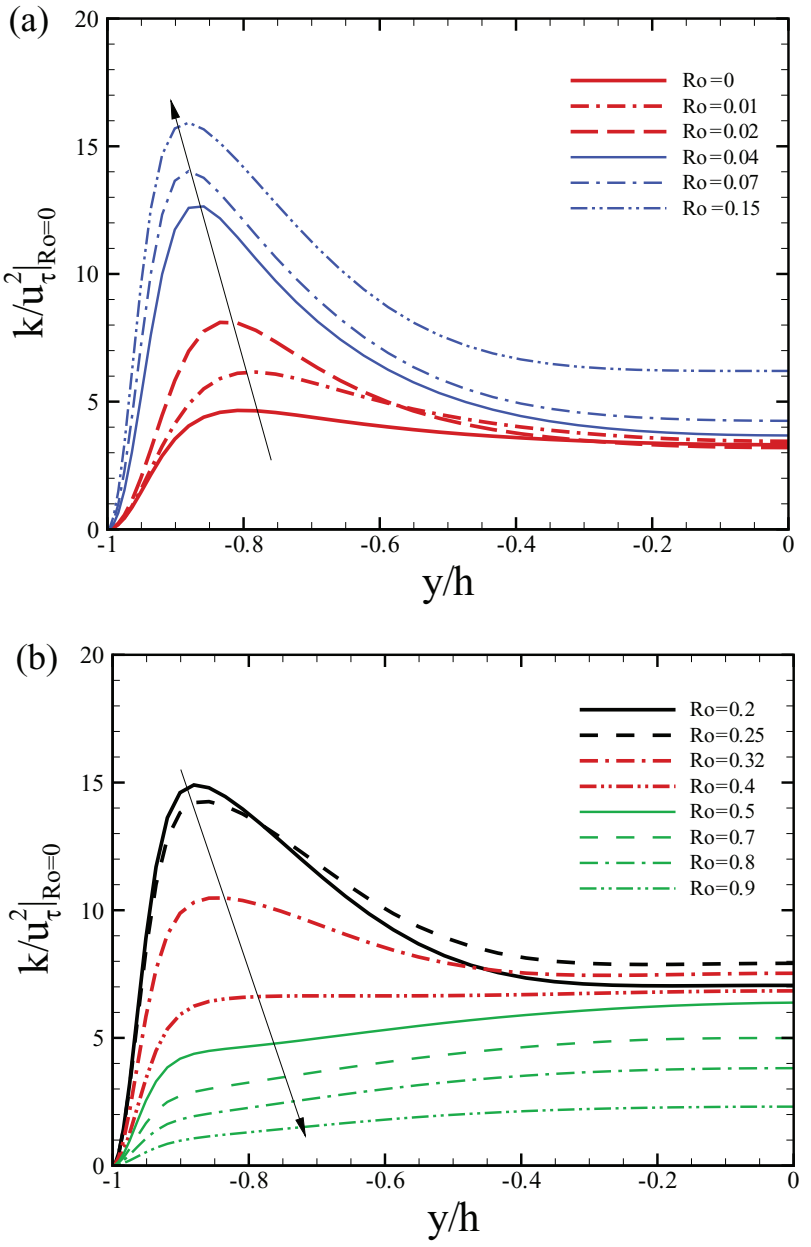

FIG. 6. Profiles of the kinetic energy with respect to total fluctuations (scaled with u_τ^2 at $\mathrm{Ro} = 0$) for (a) $0 \leqslant \mathrm{Ro} \leqslant 0.15$ and (b) $0.2 \leqslant \mathrm{Ro} \leqslant 0.9$. The arrow indicates increasing rotation number.

The terms on the left-hand sides are advection terms and the terms on the right-hand sides are production terms P, P^s, and P''; viscous dissipation terms $-\varepsilon$, $-\varepsilon^s$, and $-\varepsilon''$; and the interaction term Tr between secondary flows and turbulent fluctuations, respectively. The other terms in the square brackets are diffusion terms. Since the instantaneous Coriolis force always acts perpendicular to the instantaneous velocity vector, the Coriolis force can neither produce work nor directly alter the energy of the flow. From the transport equations (10) and (11), it is intuitively evidenced that the interaction term Tr acts as a kinetic energy bridge between the secondary flow and turbulent

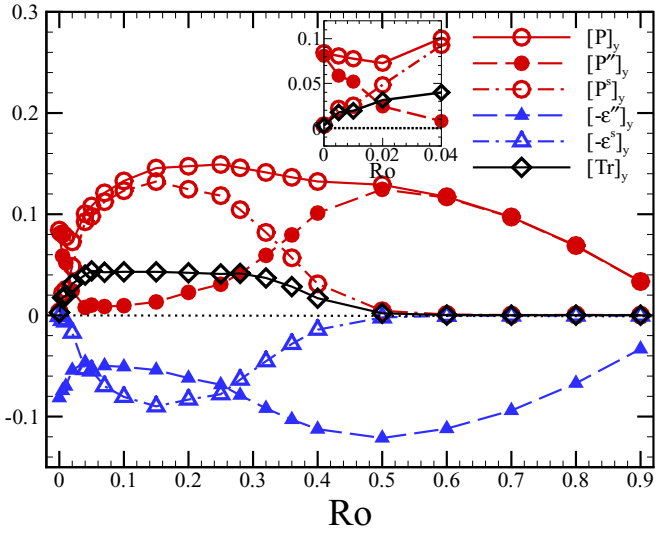

FIG. 7. Volume-averaged production terms $[P]_y$, $[P^s]_y$, and $[P'']_y$; the volume-averaged dissipation terms $[-\varepsilon^s]_y$ and $[-\varepsilon'']_y$; and the volume-averaged interaction term $[Tr]_y$ as functions of Ro. All terms are scaled with u_τ^4/ν at Ro $= 0$. The inset is the enlarged drawing for $0 \leqslant$ Ro $\leqslant 0.04$.

fluctuations, which can redistribute energy between them. The advection terms are usually very small and may be neglected. Therefore, the production terms and interaction terms can serve as net production rates and cause a local gain in the level of energy. It is reasonable to assume, as a first approximation, that effects that increase (decrease) the appropriate net production rates will also lead to an increase (decrease) in levels of energy [22].

In the present work we pay attention to the volume-averaged balance equations in a statistically stationary state, which may be helpful in studying the variations of $[k]_y$, $[k^s]_y$, and $[k'']_y$. The whole diffusion terms after the volume-averaging are quite small and can be ignored. Hence, the volume-averaged balance equations for k, k^s, and k'' become

$$0 \approx [P]_y + [-\varepsilon]_y, \tag{12}$$

$$0 \approx [P^s]_y + [-\varepsilon^s]_y + [-Tr]_y, \tag{13}$$

$$0 \approx [P'']_y + [-\varepsilon'']_y + [Tr]_y, \tag{14}$$

where $[P]_y = [P^s]_y + [P'']_y$ and $[-\varepsilon]_y = [-\varepsilon^s]_y + [-\varepsilon'']_y$. In Fig. 7 we show the volume-averaged production terms $[P]_y$, $[P^s]_y$, and $[P'']_y$; the volume-averaged dissipation terms $[-\varepsilon^s]_y$ and $[-\varepsilon'']_y$; and the volume-averaged interaction term $[Tr]_y$ as functions of Ro. The variation of $[P]_y$, the only net production rate for k, with Ro behaves similarly to the change of $[k]_y$ when $0.02 <$ Ro $\lesssim 0.9$, but it shows a different behavior when $0 \leqslant$ Ro $\lesssim 0.02$ (see the inset in Fig. 7). This is generally consistent with the assumption by Johnston *et al.* [22]. The term P can be split into two parts, i.e., P^s for k^s and P'' for k''. As shown in Fig. 7, $[P^s]_y$ is larger than $[P'']_y$ when $0.02 \lesssim$ Ro $\lesssim 0.32$ and it reveals that most of the energy from the mean flow is transferred to the secondary flow. For k^s and k'', P^s and P'' are not net production rates and we need to take the action of Tr into account. For k^s, the net production rate is $P^s - Tr$ and $[Tr]_y$ is positive (see Fig. 7), which indicates that the energy is transferred from the secondary flow to turbulent fluctuations through $-Tr$. Similar analysis can be applied to k''. The value of $[P^s]_y + [-Tr]_y$ falls to zero when Ro $\gtrsim 0.6$ and it is related to the invariant $[k^s]_y$. Note that the energy obtained from the secondary flow is larger than that gained

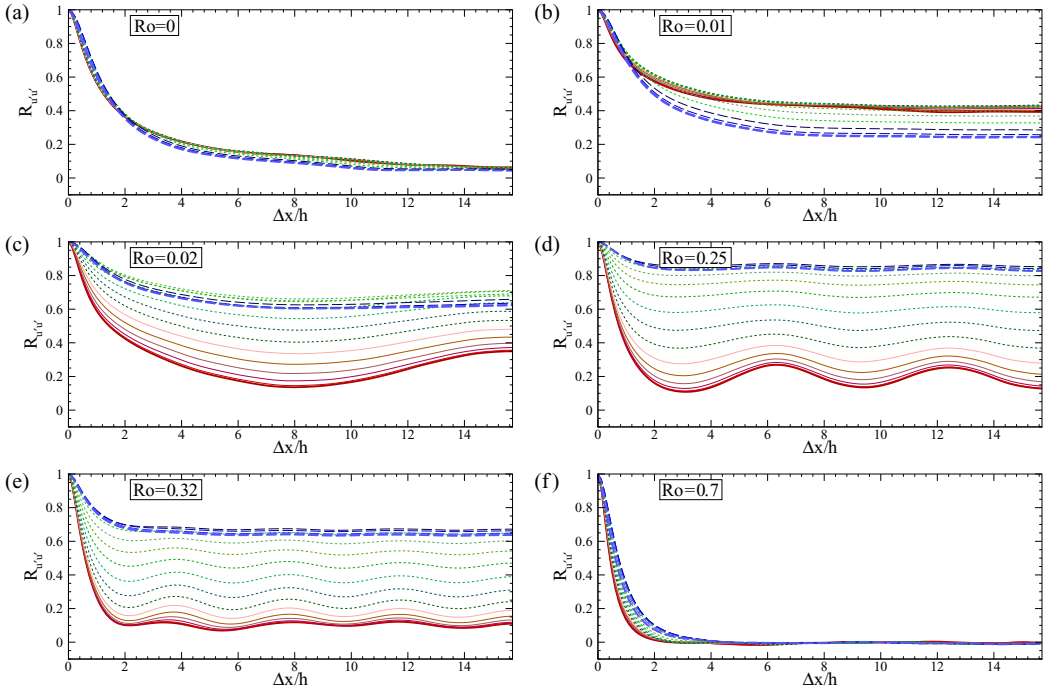

FIG. 8. Two-point streamwise correlations $R_{u'u'}(\Delta x; y)$ at different wall-normal distances: $-0.5 \lesssim y/h \lesssim 0$ (solid lines), $-0.9 \lesssim y/h \lesssim -0.5$ (dotted lines), and $-1.0 \lesssim y/h \lesssim -0.9$ (dashed lines). (a) Ro = 0, (b) Ro = 0.01, (c) Ro = 0.02, (d) Ro = 0.25, (e) Ro = 0.32, and (f) Ro = 0.7. The thick solid lines denote $y/h = 0$ and the thick dashed lines denote the first off-wall point.

from the mean shear for k'', i.e., $[Tr]_y > [P'']_y$, when $0.02 \lesssim \mathrm{Ro} \lesssim 0.28$, which indicates that the secondary flow plays a more important role in the balance of k''.

B. Flow structures

It is known that both mean flows and turbulent structures will be greatly affected by the system rotation [23]. Flow structures, which can be clearly seen from the flow visualization in experiments, are of great importance in exposing the underlying mechanism related to flow statistics. Tsukahara *et al.* [4] drew a systematic flow-regime diagram for RPCF by summarizing the observations of the experiments. However, this diagram did not cover the parameter range at $\mathrm{Re}_w = 1300$. In this subsection we will discuss the effects of rotation on flow structures by using two-point correlation functions and instantaneous flow visualizations.

To quantitatively compare the structures under different rotation numbers, the two-point streamwise correlations $R_{u'u'}(\Delta x; y)$ and spanwise correlations $R_{u'u'}(\Delta z; y)$ of u' at different wall-normal distances y/h for Ro = 0, 0.01, 0.02, 0.25, 0.32, and 0.7 are plotted in Figs. 8 and 9, respectively. The two-point streamwise and spanwise correlations for u' are defined as

$$R_{u'u'}(\Delta x; y) = \frac{\langle u'(x,y,z,t)u'(x+\Delta x,y,z,t)\rangle}{\langle u'(x,y,z,t)u'(x,y,z,t)\rangle}, \tag{15}$$

$$R_{u'u'}(\Delta z; y) = \frac{\langle u'(x,y,z,t)u'(x,y,z+\Delta z,t)\rangle}{\langle u'(x,y,z,t)u'(x,y,z,t)\rangle}. \tag{16}$$

For the nonrotating case Ro = 0, it can be observed from Fig. 8(a) that streamwise correlations at all wall-normal locations decrease monotonically with the increase of the separation distances and

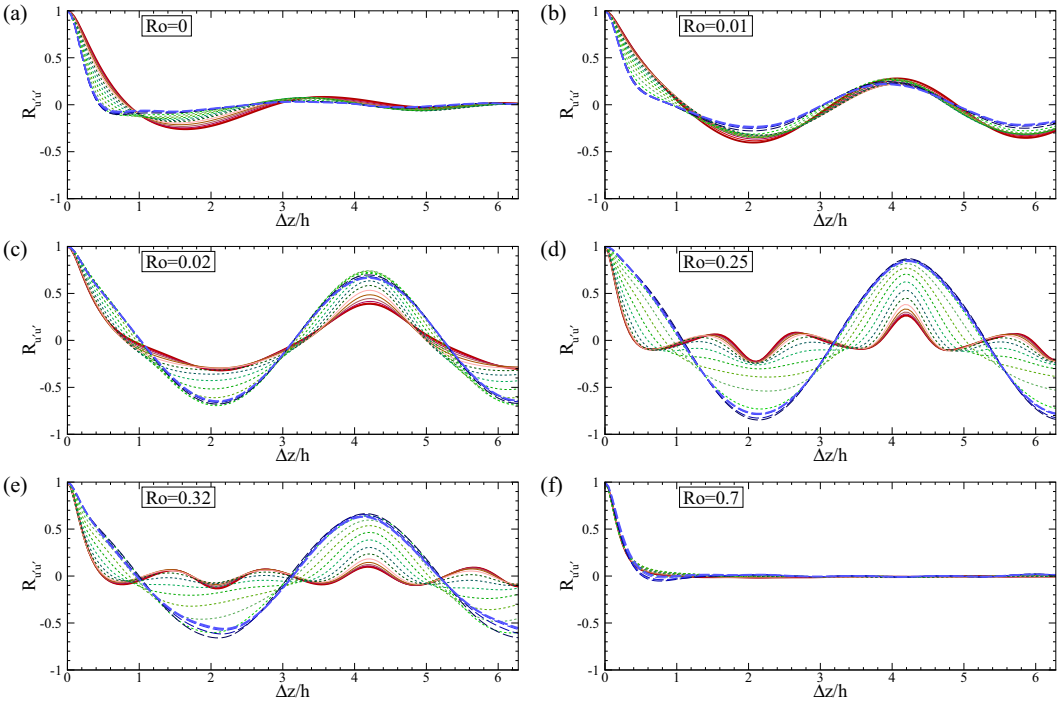

FIG. 9. Two-point spanwise correlations $R_{u'u'}(\Delta z; y)$ at different wall-normal distances: $-0.5 \lesssim y/h \lesssim 0$ (solid lines), $-0.9 \lesssim y/h \lesssim -0.5$ (dotted lines), and $-1.0 \lesssim y/h \lesssim -0.9$ (dashed lines). (a) Ro = 0, (b) Ro = 0.01, (c) Ro = 0.02, (d) Ro = 0.25, (e) Ro = 0.32, and (f) Ro = 0.7. The thick solid lines denote $y/h = 0$ and the thick dashed lines denote the first off-wall point.

they approach zero at the largest separations $\Delta x = L_x/2 \approx 15.7h$. For the spanwise correlations as shown in Fig. 9(a), no apparent periodicity can be observed as compared with the other rotating cases. At Ro = 0.01, $R_{u'u'}(\Delta x; y)$ at all wall-normal locations shown in Fig. 8(b) decrease with streamwise separations Δx and the values at the largest separations $\Delta x = L_x/2$ are much larger than zero. Moreover, the correlations in the core region are larger than those near the wall. The values of $R_{u'u'}(L_x/2; y)$ will not approach zero even though the streamwise box length is doubled. On the other hand, the two-point streamwise correlations of u'' monotonically decay to zero at $\Delta x \approx 5h$ across the channel (not shown here). Furthermore, the spanwise correlations in Fig. 9(b) show apparent periodicity. Therefore, we conjecture that secondary flows appear at this rotation rate. At Ro = 0.02, the streamwise correlations displayed in Fig. 8(c) show a different behavior. They decay with separation distance monotonically in the near wall region and the values at $\Delta x = L_x/2$ are larger than 0.6. However, in the core region, they first decay and then increase to a value around 0.4. The periodicity behavior also changes for the spanwise correlations as displayed in Fig. 9(c), where the amplitudes of the fluctuations in the near wall region are larger than those in the core region.

As the rotation number increases to Ro = 0.25, the behavior of $R_{u'u'}(\Delta x; y)$ oscillates around a value of 0.2 at the center plane as shown in Fig. 8(d). In the near wall region, the oscillation of $R_{u'u'}(\Delta x; y)$ almost disappears and the values of $R_{u'u'}(\Delta x; y)$ are around 0.8. The trend of spanwise correlations $R_{u'u'}(\Delta z; y)$ at Ro = 0.25 [see Fig. 9(d)] is a periodic variation with wavelength $\lambda_z \approx L_z/3$ in the near wall region and a composition of the periodic variation with wavelength $\lambda_z \approx L_z/3$ and a harmonic with wavelength $\lambda_z' \approx L_z/6$ in the core region. This picture is compatible with the instantaneous contours of u' at the center plane and the contours of u^s shown below in Figs. 10(d) and 11(d), respectively. The complicated characteristics of correlations indicate the complicated structures at Ro = 0.25. At a much higher rotation number Ro = 0.32, the streamwise correlations

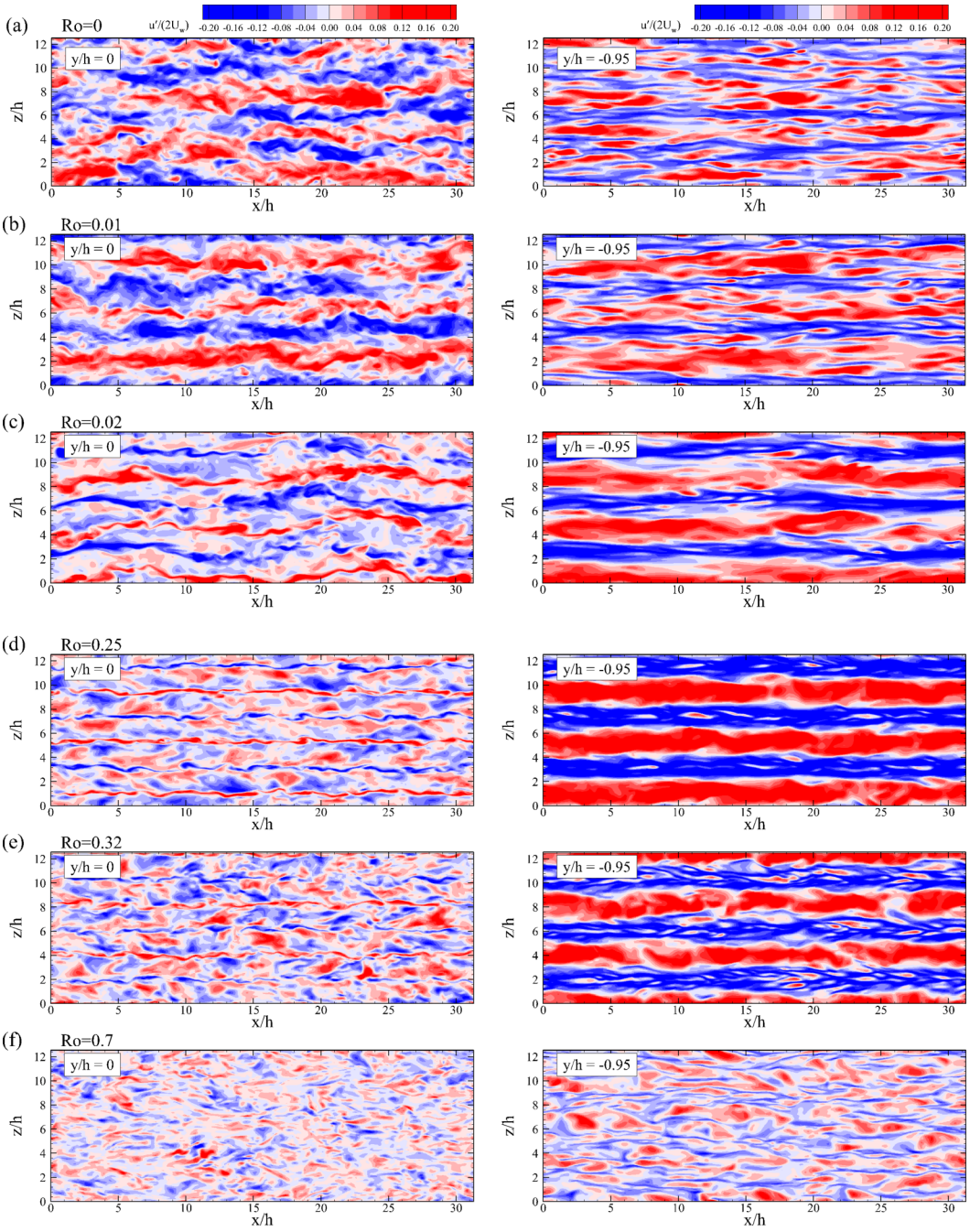

FIG. 10. Contours of $u'/2U_w$ at two different wall-parallel planes at (a) Ro = 0, (b) Ro = 0.01 (c) Ro = 0.02, (d) Ro = 0.25, (e) Ro = 0.32, and (f) Ro = 0.7. The left side is the center plane $y/h = 0$ and the right side is the near-wall plane with $y/h = -0.95$.

decrease to a value around 0.64 in the near wall region and show slight oscillation around 0.1 at the center plane [see Fig. 8(e)]. Behaviors of spanwise correlations at Ro = 0.32 appear similar to those at Ro = 0.25, except that the amplitudes at Ro = 0.32 become smaller than those at Ro = 0.25.

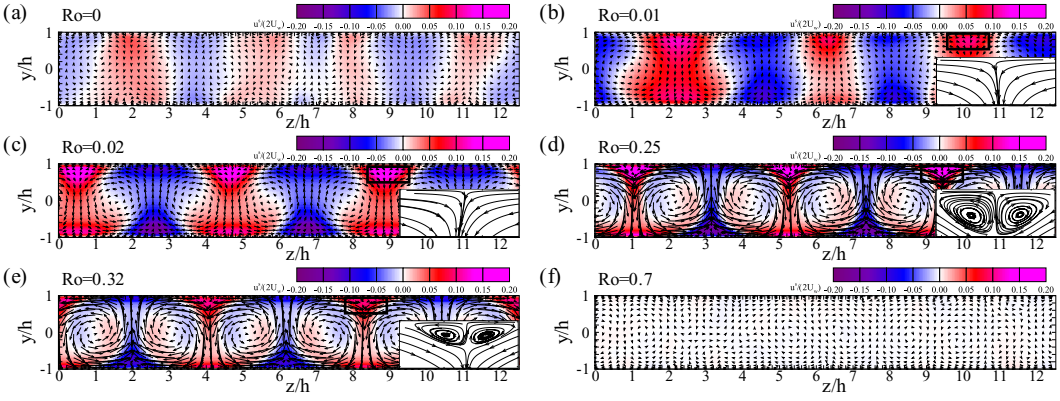

FIG. 11. Velocity vectors (v^s, w^s) of the secondary flow at (a) Ro = 0, (b) Ro = 0.01, (c) Ro = 0.02, (d) Ro = 0.25, (e) Ro = 0.32, and (f) Ro = 0.7. The vector lengths are proportional to their magnitudes. The contours show the streamwise velocity field corresponding to secondary flow. The insets in (b)–(e) are the streamlines of the secondary flow in the region of black boxes.

At Ro = 0.7, the streamwise correlations and spanwise correlations fall to zero already at small separations and remain zero as the separation increases in Figs. 8(f) and 9(f). Our results in the core region are consistent with the results reported by Barri and Andersson [8], where they indicated that the flow field with Ro = 0.7 did not possess any counterrotating roll cells.

In order to further explore the structures under different rotation numbers, we display the contours of $u'/2U_w$ at two different wall-parallel planes (center plane $y/h = 0$ and near wall plane $y/h = -0.95$) at six rotation numbers, which are Ro = 0, 0.01, 0.02, 0.25, 0.3, and 0.7, in Fig. 10, and the corresponding secondary cross-flow motions (roll cells) (v^s, w^s) and the secondary streamwise motions u^s in Fig. 11. For the nonrotating case, the corresponding contours of an instantaneous field at the center plane show that the streaks exist in the streamwise direction and are irregularly distributed in the spanwise direction compared with the rotating cases. The high-speed ($u' > 0$) and low-speed ($u' < 0$) streaks are also rather random in the near wall region. Furthermore, the secondary cross-flow motions in the nonrotating case are very weak and the streamwise motions with strength $|u^s|/U_w > 0.1$ are hardly visible in Fig. 11(a). Following the classification by Tsukahara *et al.* [4], we refer to this turbulent state as featureless turbulent flow, indicating that this flow lacks any apparent roll cells except the vortical structures. For weak rotation Ro = 0.01, the low-speed streaks are almost persistent in the streamwise direction and become uniformly distributed in the spanwise direction. It can be observed that the spacing between adjacent low-speed streaks approximately equals $L_z/3$, which is also in agreement with the streak spacing obtained from the spanwise correlations. Furthermore, the three pairs of roll cells become apparent in Fig. 11(b). Thus, we attribute the monotonic decrease and large amplitude of $R_{u'u'}(\Delta x; y)$ to the long and straight streak structures and the secondary flows in the channel. According to the roughly straight streaks and apparent roll cells, we refer to this state as turbulent flow with 2D roll cells. For Ro = 0.02, as shown in Fig. 10(c), the streaks are thin, long, and meandering at the center plane, while they are thick, long, and straight in the near wall region, which is consistent with the behavior of the streamwise correlations in Fig. 8(c). The secondary cross-flow motions and streamwise motions become evident in Fig. 11(c). Recalling the photographs from the experiments by Tsukahara *et al.* [4], we refer to this state as turbulent flow with 3D roll cells.

As the rotation number increases to Ro = 0.25, the streaks are much thinner at the center plane. Moreover, there are many random high-speed and low-speed spots between a thin, long, and straight high-speed streak and a neighboring low-speed streak. Meanwhile, the secondary cross-flow motions appear to be stronger than and asymmetric to the centerline in Fig. 11(d). We refer to this state as well-organized structures, which may correspond to the contained turbulence in roll cells by

Tsukahara *et al.* [4]. At Ro = 0.32, the contours displayed in Fig. 10(e) and the secondary cross-flow motions plotted in Fig. 11(e) are similar to those at Ro = 0.25. Therefore, the turbulent structures at Ro = 0.32 are also well organized, but their strength is weaker than that at Ro = 0.25. When the system rotates faster, for example, at Ro = 0.7, the contours at the two planes are more randomly distributed and the streamwise sizes are even smaller than those in the nonrotating case, which is consistent with the rapid falling of the streamwise and spanwise correlations at the small separations at Ro = 0.7. Furthermore, the secondary cross-flow motions will eventually weaken, as shown in Fig. 11(f), where the roll cells almost disappear and no regions with $|u^s|/U_w > 0.1$ can be detected. Combining the results by Bech and Andersson [7] and Barri and Andersson [8], we accept the fact that no roll cells exist when Ro = 0.7. Therefore, we refer to this state as turbulent flow without any roll cells in order to distinguish it from the nonrotating case.

It is noteworthy that the roll cells discussed above were also observed in turbulent Taylor-Couette flows at moderately high Taylor number [24–27] and turbulent plane Poiseuille flows with spanwise rotation [22,28–30]. In Taylor-Couette flows, these motions are interpreted as Taylor-Görtler vortices arising from the centrifugal instability mechanism associated with streamline curvature. At certain rotation rates, secondary vortex pairs can even be observed underneath two adjacent primary vortices [31]. In order to further examine the detailed secondary flow structures near the wall in the RPCF, local streamlines in the local high-speed region near the upper wall are enlarged and shown in Figs. 11(b)–11(e) for Ro = 0.01, 0.02, 0.25, and 0.32, respectively. At lower rotation numbers Ro = 0.01 and 0.02, where the secondary flows are not strong enough, no secondary vortex pairs can be observed near the upper high-speed region. On the other hand, for Ro = 0.25 and 0.32, secondary vortex pairs can be identified clearly, which are very similar to those in the Taylor-Couette flows [31]. In fact, these secondary vortex pairs in the region near the upper and lower walls can be discerned when $0.07 \lesssim \mathrm{Ro} \lesssim 0.36$ according to our simulations. Through the secondary cross-flow motions displayed in Fig. 11, we may infer that the roll cells are strengthened with the system rotation for $\mathrm{Ro} \leqslant 0.25$ and then weakened when $\mathrm{Ro} > 0.25$, which is in agreement with the results of $[k^s]_y$ shown in Fig. 5. It is very interesting to note that u^s is not uniformly distributed in the cross section, but is concentrated in certain regions between roll-cell pairs. The low-speed regions are stronger near the bottom wall, while the high-speed zones are stronger near the top wall. If the roll cells become stronger, the regions with a higher value of $|u^s|$ are more evidently concentrated. At Ro = 0.25 and 0.32, as depicted in Figs. 11(d) and 11(e), respectively, the regions with $-0.05 < u^s/2U_w < 0$ and $0 < u^s/2U_w < 0.05$ wedge into each other in the center region of the roll cells, which may be related to strong and complicated flow structures.

Further insight into the features of the turbulent structures can be obtained by using 3D visualizations of the vortical structures. The instantaneous distributions of the small-scale vortices are represented by isosurfaces of $Qh^2/U_w^2 \geqslant 1.0$ (here $Q = -\frac{\partial u_i'}{\partial x_j}\frac{\partial u_j'}{\partial x_i}$ [32]) and the results at Ro = 0, 0.01, 0.02, 0.25, and 0.7 are shown in Fig. 12. For the nonrotating case [see Fig. 12(a) and [33]], the small-scale vortices fill the whole channel randomly. Most of these vortices are confined to one side of the walls and very few of them penetrate the central plane, as indicated by the side view depicted in Fig. 13(a). For the weak rotation Ro = 0.01, as shown in Fig. 12(b) and [33], the small-scale vortices lose their behaviors of random distribution and begin to cluster, forming bunches alternatively distributed in the upper half and lower half of the channel in the spanwise direction. Furthermore, the bunches of vortices in the upper half channel are located over the high-speed streaks and those in the lower half channel are clustered over the low-speed streaks. The vortices are still confined to the local walls and few of them penetrate the central plane as those in nonrotating case [see Fig. 13(b)]. We believe that this alternant behavior of the clusters of vortices is associated with the 2D roll cells. It is particularly noteworthy that the small-scale vortices at Ro = 0.01 are sparser than those from the nonrotating case. This is consistent with the fact that the turbulent fluctuations are suppressed due to system rotation as shown in Fig. 5.

When the system rotates a little faster to reach Ro = 0.02, the distribution of 3D small-scale vortices changes again and two instantaneous fields with a time interval of $0.287L_x/U_w$ are shown

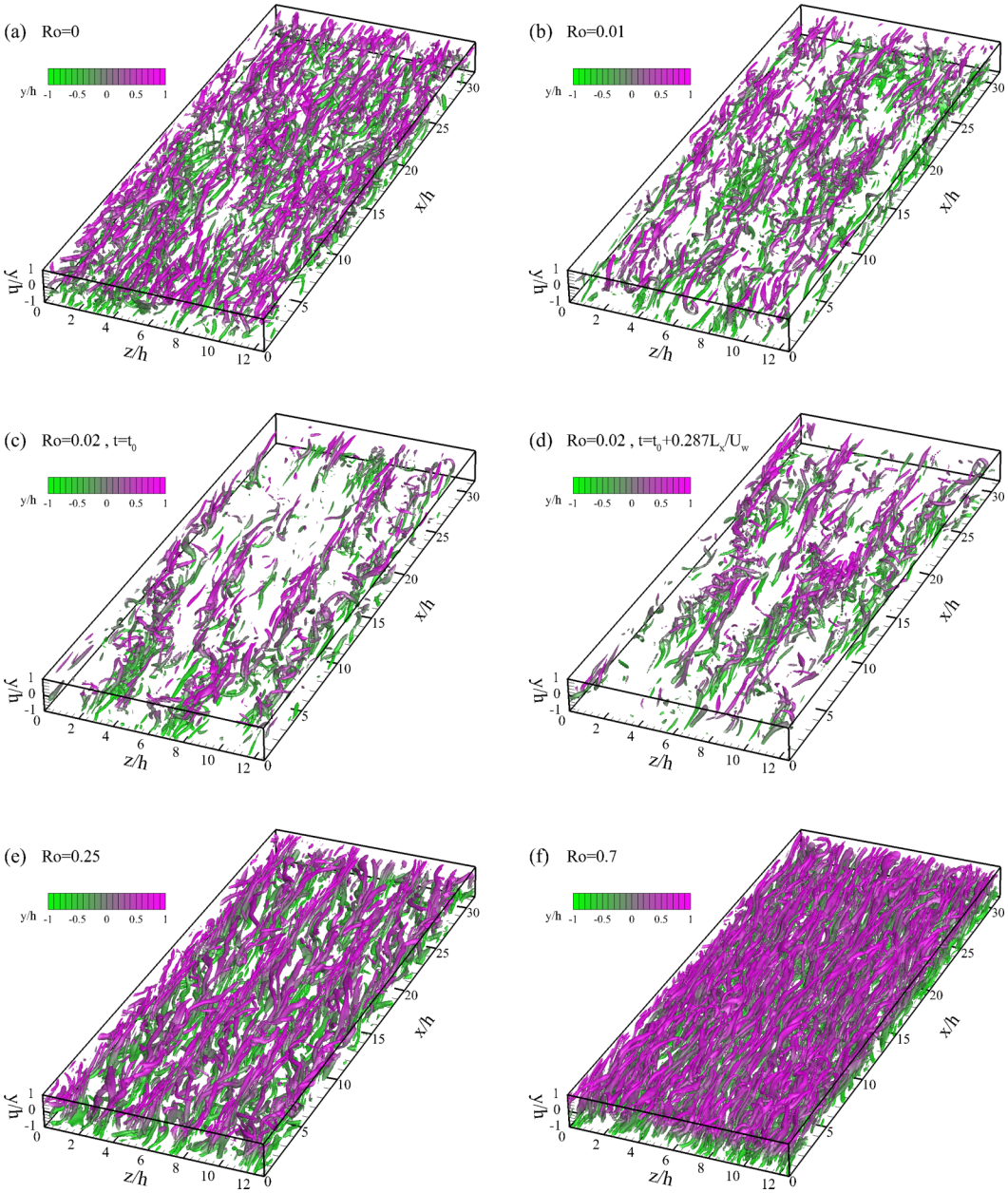

FIG. 12. Instantaneous 3D flow structures shown by isosurfaces of $Qh^2/U_w^2 \geqslant 1.0$: (a) Ro = 0, (b) Ro = 0.01, (c) and (d) Ro = 0.02 at two different time steps with the interval $0.287L_x/U_w$, (e) Ro = 0.25, and (f) Ro = 0.7. The isosurfaces are colored by y/h.

in Figs. 12(c) and 12(d) (see also [33]). It can be clearly seen that the clusters of small-scale vortices in these two instantaneous fields are not as straight in the streamwise direction as those at Ro = 0.01. Instead, the clusters are meandering in the streamwise direction and a bifurcation can also be observed. The location of the bifurcation moves forward as time passes. From the side views shown in Figs. 13(c) and 13(d), these small-scale vortices tend to move away from the wall and some of them penetrate the central plane. We attribute these flow structures to the 3D roll cells.

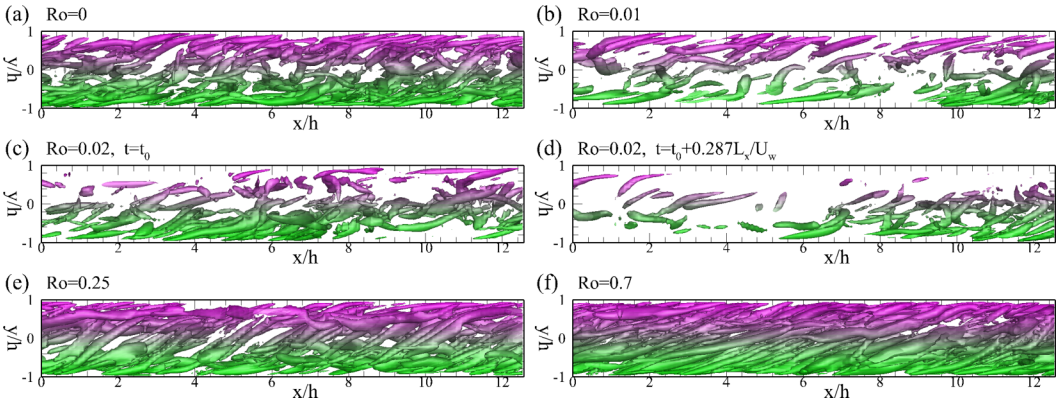

FIG. 13. Side views of 3D flow structures shown in Fig. 12 in a subdomain with $0 \leqslant x/h \leqslant 4\pi$ and $0 \leqslant z/h \leqslant 4$.

As the rotation number increases to $\mathrm{Ro} = 0.25$, another different behavior of the small-scale vortices can be observed from Fig. 12(e) (see also [33]). These vortices are well organized and stable in time. The vortices are herringbonelike and clustered between streaks from top view of 3D flow visualization, forming annuluses from the front view (not shown). The herringbonelike structure was used by Dong [34] to describe the spatial-temporal characteristics of the azimuthal velocity streaks in Taylor-Couette flows. As shown in Fig. 13(e), most of these vortices gather near one of the walls, penetrate the central plane, and extend to the other wall. The behavior of small-scale vortices is associated with the well-organized motions of roll cells and it can be observed for $0.07 \lesssim \mathrm{Ro} \lesssim 0.36$.

For the strong rotation $\mathrm{Ro} = 0.7$ shown in Fig. 12(f), where the roll cells disappear, the vortices fill the whole channel like those in the nonrotating case, but with a much denser distribution (see [33]). A striking difference between the flow structures in the nonrotating case and those at $\mathrm{Ro} = 0.7$ can be clearly seen from Figs. 13(a) and 13(f), where most of the vortices in the latter case start from the lower wall, penetrate the central plane, and extend to the upper wall like those at $\mathrm{Ro} = 0.25$.

IV. CONCLUSION

In the present work a series of DNSs of spanwise-rotating plane Couette flows at a Reynolds number of 1300 with rotation numbers Ro between 0 and 0.9 was carried out to investigate the effects of the destabilizing rotation on turbulent statistics and flow structures. Based on the comparisons with the previously published results at several rotation numbers and our simulations with larger computational domain and finer grid resolution, we have demonstrated that our simulations are correct and reliable.

We studied the variations of several typical turbulent statistics as functions of Ro, including the mean shear rate at the centerline Ψ, wall-friction Reynolds number Re_τ, and volume-averaged kinetic energies with respect to the secondary flow field $[k^s]_y$, the turbulent field $[k'']_y$, and the total fluctuation field $[k]_y$. Our results show that these quantities arrive at their extreme values at different Ro. For Ψ, the value first decreases with Ro and then increases with Ro and the minimum is located around $\mathrm{Ro} = 0.02$. For Re_τ, the opposite trend is observed with the maximum located at $\mathrm{Ro} = 0.15$. The variation of $[k]_y$ shows that the rotation first enhances the total fluctuations when $\mathrm{Ro} \leqslant 0.25$ and then suppresses them when $\mathrm{Ro} > 0.25$. The kinetic energy of the secondary flow $[k^s]_y$ plays a dominant role when $0.02 \lesssim \mathrm{Ro} \lesssim 0.36$ and the contribution of the secondary flow to the kinetic energy of the total fluctuations reaches saturation level when $0.07 \lesssim \mathrm{Ro} \lesssim 0.25$. The secondary flow is fully suppressed by the strong system rotation when $\mathrm{Ro} \gtrsim 0.7$.

We analyzed the terms in volume-averaged balance equations for $[k]_y$, $[k^s]_y$, and $[k'']_y$, which is helpful in studying the variations of kinetic energy. The change of $[k]_y$ with Ro is consistent

with the variation of the net production rate $[P]_y$ in most of the rotation number range studied. The interaction term acts like a kinetic energy bridge that transfers energy from the secondary flow to turbulent fluctuations. Furthermore, for k'', the energy obtained from the secondary flow is larger than that gained from the mean shear, i.e., $[Tr]_y > [P'']_y$, when $0.02 \leqslant \mathrm{Ro} \leqslant 0.28$, which indicates that the secondary flow plays a more important role in the balance of k''.

The variations of flow structures are closely related to the changes of turbulent statistics. The two-point streamwise and spanwise correlations of the streamwise total fluctuation velocity and 2D and 3D flow visualizations are used to identify the flow structures. In the nonrotating case, the streamwise correlations in the whole channel show the same behavior and decrease monotonically and approach zero at the largest separations. Furthermore, the streaks and vortices are distributed irregularly. Therefore, the flow in the nonrotating case is featureless owing to a lack of obvious roll cells in comparison to the rotating cases. For weak and moderate rotations $0.01 \lesssim \mathrm{Ro} \lesssim 0.36$, the correlations in the core region present features different from those near the wall and the magnitude of the correlation function is associated with the strength of the streaks. In particular, the apparent periodicity of spanwise correlations for $0.01 \lesssim \mathrm{Ro} \lesssim 0.36$ demonstrates the existence of roll cells. For weak rotation $\mathrm{Ro} = 0.01$, the monotonic decrease of streamwise correlations indicates that the 2D roll cells occur. Moreover, the clusters of vortices show alternant behavior in the spanwise direction and few vortices penetrate the central plane. For the weak rotation $\mathrm{Ro} = 0.02$, the streamwise correlations in the core region first decay and then increase, which indicates there are 3D roll cells. Furthermore, through 3D flow visualization, the clusters of vortices are meandering in the streamwise direction and a bifurcation can also be observed, which is connected with the 3D roll cells. For the moderate rotation $\mathrm{Ro} = 0.25$, the flow structures become more complicated. First, the streamwise correlations oscillate in the core region and the variation of spanwise correlations is composed of a periodic variation with a wavelength of $L_z/3$ and a harmonic with a wavelength of $L_z/6$ in the core region. Second, the secondary vortex pairs coexist with the roll cells through the investigation of the secondary flow; they are presented in the region near the walls. Finally, in the 3D flow visualization, the herringbonelike vortices are clustered between streaks from the top view and form annuluses from the front view. In the present work, we refer to these flow structures as well-organized structures, which occur when $0.07 \lesssim \mathrm{Ro} \lesssim 0.36$ in our simulations. For the strong rotation $\mathrm{Ro} = 0.7$, the streamwise correlations and spanwise correlations fall to zero already at small separations, so it can be deduced that there are no roll cells. The vortices fill the whole channel like those in the nonrotating case, which attributes to the disappearance of roll cells, while the vortices penetrate the central plane.

ACKNOWLEDGMENTS

Numerical simulations were realized at the Dawn cluster in Peking University, China. We acknowledge financial support provided by National Natural Science Foundation of China (Grants No. 11521091, No. 11272013, and No. 11302006). The authors would like to thank Professor Jian Su and Professor Kun Xu for many useful discussions and suggestions.

[1] N. Tillmark and P. H. Alfredsson, in *Advances in Turbulence VI*, edited by S. Gavrilakis, L. Machiels, and P. A. Monkewitz (Kluwer, Dordrecht, 1996), pp. 391–394.

[2] P. H. Alfredsson and N. Tillmark, in *Laminar Turbulent Transition and Finite Amplitude Solutions*, edited by T. Mullin and R. R. Kerswell (Springer, Berlin, 2005), pp. 173–193.

[3] K. Hiwatashi, P. H. Alfredsson, N. Tillmark, and M. Nagata, Experimental observations of instabilities in rotating plane Couette flow, Phys. Fluids **19**, 048103 (2007).

[4] T. Tsukahara, N. Tillmark, and P. H. Alfredsson, Flow regimes in a plane Couette flow with system rotation, J. Fluid Mech. **648**, 5 (2010).

[5] K. H. Bech and H. I. Andersson, in *Advances in Turbulence VI* (Ref. [1]), pp. 91–94.

[6] K. H. Bech and H. I. Andersson, Secondary flow in weakly rotating turbulent plane Couette flow, J. Fluid Mech. **317**, 195 (1996).
[7] K. H. Bech and H. I. Andersson, Turbulent plane Couette flow subject to strong system rotation, J. Fluid Mech. **347**, 289 (1997).
[8] M. Barri and H. I. Andersson, Computer experiments on rapidly rotating plane Couette flow, Commun. Comput. Phys. **7**, 683 (2010).
[9] T. Tsukahara, Structures and turbulent statistics in a rotating plane Couette flow, J. Phys.: Conf. Ser. **318**, 022024 (2011).
[10] M. Salewski and B. Eckhardt, Turbulent states in plane Couette flow with rotation, Phys. Fluids **27**, 045109 (2015).
[11] J. Kim, P. Moin, and R. Moser, Turbulence statistics in fully developed channel flow at low Reynolds number, J. Fluid Mech. **177**, 133 (1987).
[12] S. Gavrilakis, H. M. Tsai, P. R. Voke, and D. C. Leslie, in *Direct and Large Eddy Simulation of Turbulence*, Notes on Numerical Fluid Mechanics Vol. 15, edited by U. Schumann and R. Friedrich (Vieweg, Braunschweig, 1986), pp. 105–118.
[13] M. Manhart, A zonal grid algorithm for DNS of turbulent boundary layers, Comput. Fluids **33**, 435 (2004).
[14] K. H. Bech and H. I. Andersson, in *Direct and Large-Eddy Simulation II*, edited by P. R. Voke, L. Kleiser, and J. P. Chollet (Kluwer, Dordrecht, 1994), pp. 13–24.
[15] R. D. Moser and P. Moin, The effects of curvature in wall-bounded turbulent flows, J. Fluid Mech. **175**, 479 (1987).
[16] M. J. Lee and J. Kim, in *Proceedings of the Eighth Symposium on Turbulent Shear Flows*, edited by F. Durst, R. Friedrich, B. E. Launder, F. W. Schmidt, U. Schumann, and J. H. Whitelaw (Springer, Berlin, 1991), paper 5-3.
[17] T. Kawata and P. H. Alfredsson, Turbulent rotating plane Couette flow: Reynolds and rotation number dependency of flow structure and momentum transport, Phys. Rev. Fluids **1**, 034402 (2016).
[18] P. Bradshaw, The analogy between streamline curvature and buoyancy in turbulent shear flow, J. Fluid Mech. **36**, 177 (1969).
[19] A. Suryadi, A. Segalini, and P. H. Alfredsson, Zero absolute vorticity: Insight from experiments in rotating laminar plane Couette flow, Phys. Rev. E **89**, 033003 (2014).
[20] T. Kawata and P. H. Alfredsson, Experiments in rotating plane Couette flow—Momentum transport by coherent roll-cell structure and zero-absolute-vorticity state, J. Fluid Mech. **791**, 191 (2016).
[21] Z. H. Xia, Y. P. Shi, and S. Y. Chen, Direct numerical simulation of turbulent channel flow with spanwise rotation, J. Fluid Mech. **788**, 42 (2016).
[22] J. P. Johnston, R. M. Halleen, and D. K. Lezius, Effects of spanwise rotation on the structure of two-dimensional fully developed turbulent channel flow, J. Fluid Mech. **56**, 533 (1972).
[23] J. P. Johnston, Effects of system rotation on turbulence structure: A review relevant to turbomachinery flows, Int. J. Rotat. Mach. **4**, 97 (1998).
[24] A. Barcilon and J. Brindley, Organized structures in turbulent Taylor-Couette flow, J. Fluid Mech. **143**, 429 (1984).
[25] C. D. Andereck, S. S. Liu, and H. L. Swinney, Flow regimes in a circular Couette system with independently rotating cylinders, J. Fluid Mech. **164**, 155 (1986).
[26] T. Wei, E. M. Kline, S. H.-K. Lee, and S. Woodruff, Görtler vortex formation at the inner cylinder in Taylor-Couette flow, J. Fluid Mech. **245**, 47 (1992).
[27] S. Grossmann, D. Lohse, and C. Sun, Highcreynolds number Taylor-Couette turbulence, Annu. Rev. Fluid Mech. **48**, 53 (2016).
[28] R. Kristoffersen and H. I. Andersson, Direct simulations of low-Reynolds-number turbulent flow in a rotating channel, J. Fluid Mech. **256**, 163 (1993).
[29] E. Lamballais, O. Métais, and M. Lesieur, Spectral-dynamic model for large-eddy simulations of turbulent rotating channel flow, Theor. Comput. Fluid Dyn. **12**, 149 (1998).
[30] O. Grundestam, S. Wallin, and A. V. Johansson, Direct numerical simulations of rotating turbulent channel flow, J. Fluid Mech. **598**, 177 (2008).

[31] M. Bilson and K. Bremhorst, Direct numerical simulation of turbulent Taylor-Couette flow, J. Fluid Mech. **579**, 227 (2007).

[32] N. Kasagi, Y. Sumitani, Y. Suzuki, and O. Iida, Kinematics of the quasi-coherent vortical structure in near-wall turbulence, Int. J. Heat Fluid Flow **16**, 2 (1995).

[33] See Supplemental Material at http://link.aps.org/supplemental/10.1103/PhysRevFluids.1.054401 for movies.

[34] S. Dong, Direct numerical simulation of turbulent Taylor-Couette flow, J. Fluid Mech. **587**, 373 (2007).